High-resolution spatiotemporal reconstruction of complex fields in optical turbulence uncovers departures from Gaussian statistics: supplemental document

The following sections provide further illustration to the description given in the main article.

1. EXPERIMENTAL RESULTS: ADDITIONAL RECONSTRUCTION SAMPLES AND VISUALIZATIONS

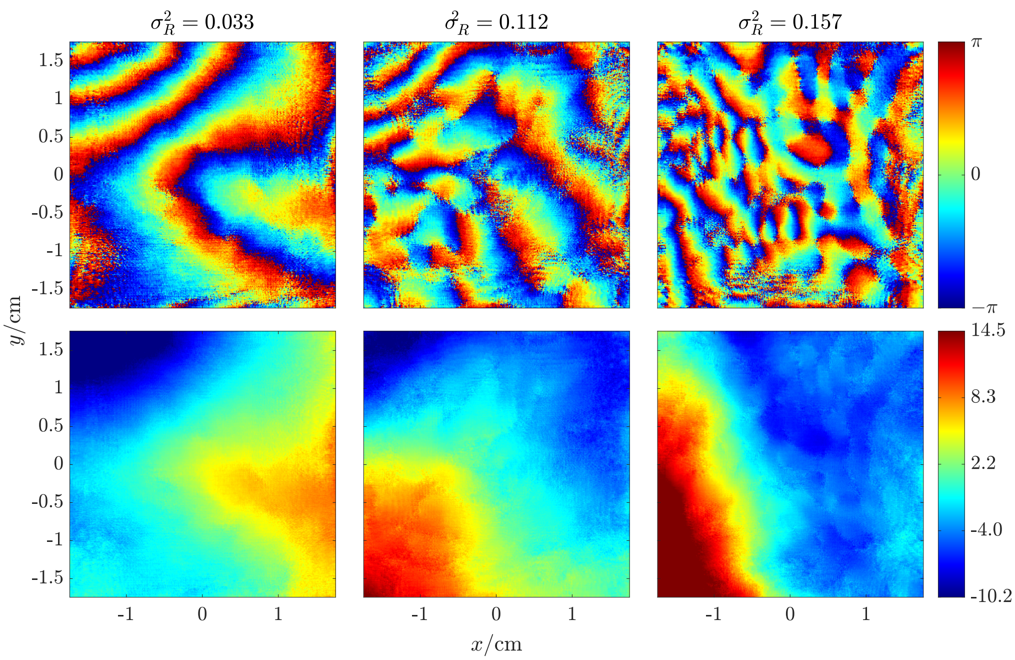

Fig. S1. Representative samples of experimental spatial phase reconstructions for three turbulence strengths. Wrapped (top row) and unwrapped (bottom row) phase maps are shown for the first, second, and third columns, corresponding to increasing turbulence strength as indicated by the Rytov variance σ_R^2 in the column headers. Frame indices correspond to independent realizations within each acquisition sequence. The corresponding spatiotemporal evolution of the reconstructed wavefronts is provided in Supplementary Visualizations 1–3.

The purpose of these samples is to illustrate the spatiotemporal resolution and dynamic range of the reconstruction technique across different turbulence strengths, complementing the results presented in the main text.

These examples highlight the increasing spatial complexity of the reconstructed phase with turbulence strength, while preserving fine-scale structure within individual coherence cells.

In addition to the static phase maps, the full temporal evolution of the reconstructed wavefronts is provided as Supplementary Visualizations 1–3. Each visualization corresponds to one of the turbulence conditions shown in Fig. S1 and displays the optical path difference (OPD) dynamics derived from consecutive reconstructed frames acquired at 1000 Hz and rendered at 30 fps. These slow-motion visualizations preserve the temporal continuity of the measurements and demonstrate the reconstruction method's ability to capture turbulence-driven phase dynamics over extended time intervals.

2. COHERENCE ELLIPSES: ELLIPTICITY AND ORIENTATION

In the main text, spatial coherence is characterized through the analysis of e^{-1} isocoherence contours extracted from the measured degree of coherence maps. These contours are fitted with ellipses to quantify anisotropy and to define an effective coherence radius $\rho_0 = \sqrt{\rho_{\min}\rho_{\max}}$, where $\rho_{\min}$ and $\rho_{\max}$ denote the semi-minor and semi-major axes, respectively.

Figure S2 summarizes additional parameters obtained from these ellipse fits, namely the ellipticity and the orientation angle, for both the directly estimated degree of coherence (DOC) and the normal degree of coherence (NDOC) derived under the Gaussian hypothesis. Each point corresponds to an independent turbulence condition, and shaded regions indicate the associated confidence intervals.

The results show that, while both DOC- and NDOC-based estimates exhibit increasing anisotropy with decreasing coherence radius, systematic differences arise between the two approaches. In particular, NDOC-based estimates tend to underestimate ellipticity and display reduced sensitivity to variations in the orientation angle compared to DOC. These discrepancies are consistent with the assumption of Gaussian phase statistics underlying NDOC and highlight the loss of directional information when coherence is inferred solely from second-order phase statistics.

These additional parameters support the conclusions drawn in the main text by demonstrating that departures between DOC and NDOC extend beyond coherence radius estimates and also affect anisotropy metrics derived from the coherence structure.

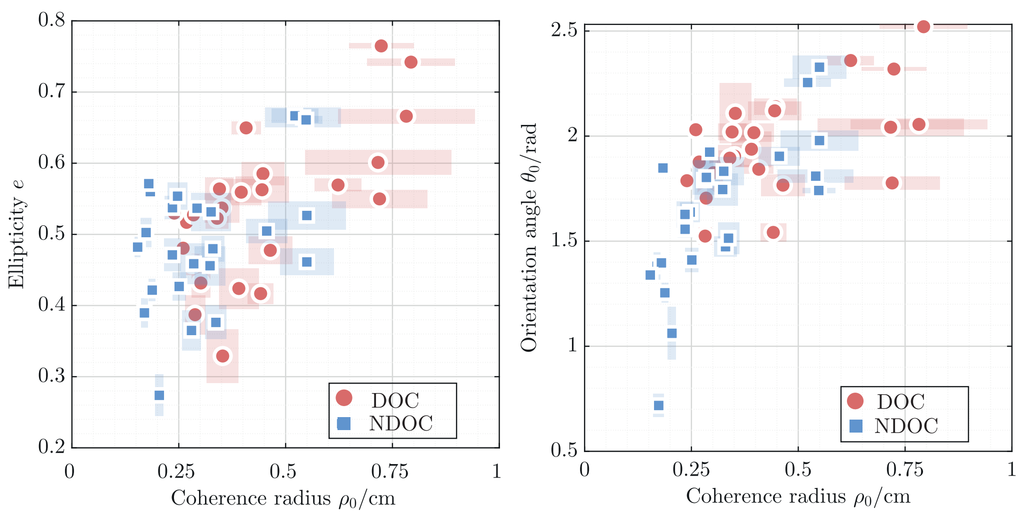

Fig. S2. Ellipticity (left) and orientation angle (right) of the coherence ellipses derived from fits to the e^{-1} isocoherence contours. Results are shown for coherence estimates based on the directly measured degree of coherence (DOC, red circles) and the normal degree of coherence (NDOC, blue squares). Each point represents an independent turbulence condition, and shaded regions indicate the corresponding confidence intervals. Ellipse parameters are plotted as a function of the effective coherence radius $\rho_0 = \sqrt{\rho_{\min}\rho_{\max}}$, where $\rho_{\min}$ and $\rho_{\max}$ denote the semi-minor and semi-major axes, respectively.

3. IMPACT OF THE UNWRAPPING METHOD ON STATISTICAL ESTIMATES

Phase unwrapping can alter the statistical properties of a complex optical field and introduce biases into coherence estimates derived from phase-based metrics, making the preservation of statistical integrity a critical requirement for any quantitative comparison among coherence models.

To assess the impact of the unwrapping procedure on the estimated field statistics, we use the mutual intensity function to compute the degree of coherence directly from the complex field, without requiring phase unwrapping. This estimate serves as a reference independent of any

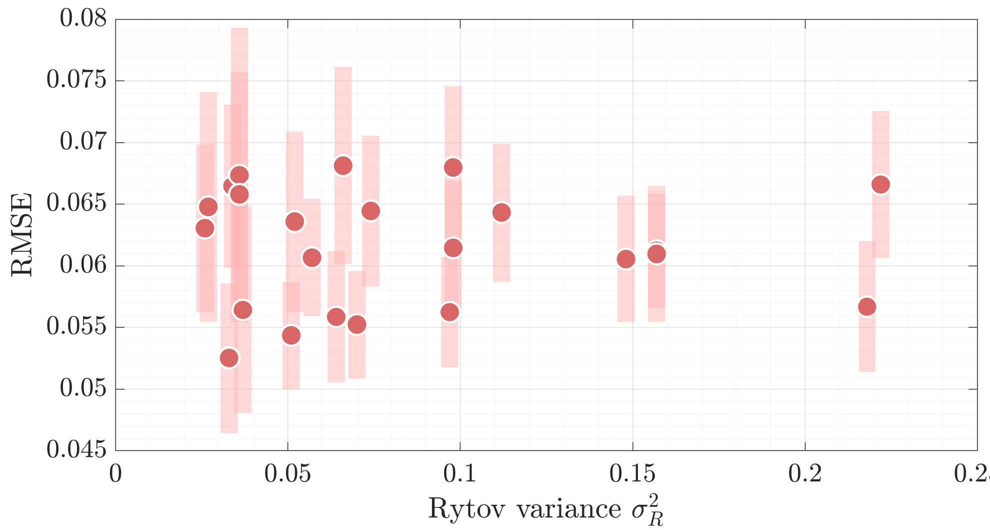

Fig. S3. Root-mean-square error (RMSE) between coherence estimates derived from the mutual intensity function before and after phase unwrapping, evaluated across all turbulence conditions. The RMSE is plotted as a function of the Rytov variance σ_R^2. Error bars indicate measurement uncertainty. The consistently low RMSE ($< 7\%$) and the absence of a systematic dependence on turbulence strength indicate that the phase unwrapping procedure preserves the statistical properties of the reconstructed complex field.

assumptions inherent in unwrapping or in phase-based statistical models. We then compare this reference with coherence estimates obtained from the same reconstructed field after phase unwrapping.

Figure S3 shows the root-mean-square error (RMSE) between the degree of coherence computed from the mutual intensity function before and after phase unwrapping, evaluated across all turbulence conditions and expressed as a function of the Rytov variance σ_R^2. The RMSE remains below 7% across all cases and shows no systematic increase with turbulence strength.

These results demonstrate that the phase unwrapping procedure preserves the statistical properties of the reconstructed complex field with high degree. Consequently, the discrepancies observed between coherence estimates based on the direct degree of coherence and those derived under the Gaussian hypothesis cannot be attributed to artifacts introduced by the unwrapping process.

4. END-TO-END CALIBRATION OF THE MEASUREMENT PIPELINE

The complex-field reconstruction algorithm was validated against objects with known amplitude and phase in Peters et al., *Opt. Lett.* **42**, 2030 (2017) and Romero et al., *Opt. & Laser Technol.* **191**, 113311 (2025), including a calibrated lens, a USAF 1951 resolution target, a portrait from the Kodak dataset, and two Zernike mode combinations (primary spherical aberration and oblique trefoil), yielding phase reconstruction errors below 1% under low-noise conditions.

As an end-to-end calibration of the full measurement pipeline, Fig. S4 shows the spatial map and radial profile of the degree of coherence measured with the turbulence generator inactive. The DOC is spatially uniform throughout the pupil, declining gently from 0.955 at the center to 0.89 at the edge, with a pupil-averaged value of 0.933 ± 0.017. This profile reflects the intrinsic spatial coherence of the laser source and relay optics; it is static across all turbulence conditions and is divided out of both DOC and NDOC before comparison, as described in Methods. The residual departure from unity is negligible compared to the coherence drops of more than 60% induced by active turbulence, confirming that the optical relay, reconstruction algorithm, and coherence estimation procedure introduce no systematic bias into the reported coherence metrics.

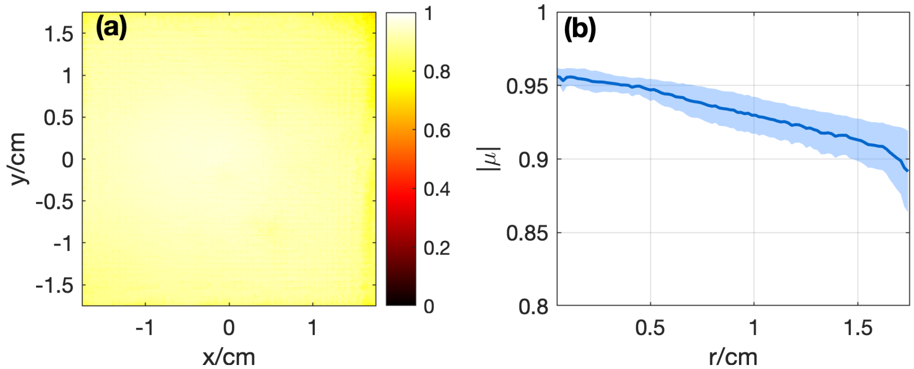

Fig. S4. Reference degree of coherence measured with the turbulence generator inactive. (a) Spatial map of $|\mu|$ across the pupil. (b) Radial profile of $|\mu|$ averaged over concentric rings. Shaded region indicates ± 1 standard deviation. The DOC is 0.933 ± 0.017 across the pupil, confirming that the measurement pipeline introduces no systematic bias into the coherence estimates.